Applied Surface Science 593 (2022) 153317

Contents lists available at ScienceDirect

Applied Surface Science

journal homepage: www.elsevier.com/locate/apsusc

Full length article

First-principles study of two-dimensional $MoN_2X_2Y_2$ (X=B~In, Y=N~Te) nanosheets: The III–VI analogues of $MoSi_2N_4$ with peculiar electronic and magnetic properties

Yi Ding [a,*], Yanli Wang [b,*]

[a] School of Physics, Hangzhou Normal University, Hangzhou, Zhejiang 311121, People's Republic of China
[b] Department of Physics, Zhejiang Sci-Tech University, Hangzhou, Zhejiang 310018, People's Republic of China

ARTICLE INFO

Keywords:
MoA_2Z_4
Layered material
Electronic structure
First-principles calculations

ABSTRACT

The recent discovery of $MoSi_2N_4$ nanosheet boosts researches on the layered MA_2Z_4 materials. Utilizing first-principles calculations, we investigate the isoelectronic and isostructural analogues of $MoSi_2N_4$, i.e. group III–VI $MoN_2X_2Y_2$ (X=B~In, Y=N~Te) nanosheets. Nine III–VI XY combinations are revealed to form stable $MoN_2X_2Y_2$ systems with robust dynamical, thermal and energetic stability. They can be indirect-gap semiconductors or metals depending on the XY compositions. There is a linear relationship between the gap size and lattice constant of semiconducting $MoN_2X_2Y_2$ systems. More interestingly, a Mexican-hat-like band dispersion appears in the top valence band of $MoN_2X_2Y_2$ (XY=AlO, GaO, InO) nanosheets, for which the hole doping can induce Stoner ferromagnetism and convert the systems into half-metals. For the van der Waals heterostructures formed by $MoN_2X_2Y_2$ (XY=BS, AlO) and $MoSi_2N_4$ nanosheets, they exhibit versatile and strain-tunable band alignments, including the straddling-gap type-I, staggered-gap type-II, and broken-gap type-III ones. Our study demonstrates that the composition of surface layers is a new degree to manipulate the electronic structure of MA_2Z_4-based materials and it will bring tunable electronic and magnetic behaviours for the electrics, spintronics, and nano-device applications.

1. Introduction

Layered transition-metal (TM) systems, including dichalcogenides (TMDs [1,2]), dinitrides (TMDNs [3,4]), diborides (TMDBs [5,6]), dihydrides (TMDHs [7,8]), as well as carbides and nitrides (MXenes [9,10]), are a plethora of two-dimensional (2D) materials with promising electronic and magnetic properties. Very recently, a new member of layered materials, i.e. 2D $MoSi_2N_4$ system, has been synthesized in the chemical vapour deposition experiment [11]. This discovery boosts researches on the layered MA_2Z_4 materials, where M belongs to the 4d/5d TM elements, A is the Si or Ge element, and Z stands for N, P, As ones [12]. The $MoSi_2N_4$ nanosheet possesses a semiconducting property like the MoS_2 system [13,14], which also exhibits the spin-valley coupling electronic and optical behaviours [15–17]. Particular physical properties, including large piezoelectricity [18,19], high lattice thermal conductivity [20,21], high-efficient electrocatalytic activity [22–24], and good molecular detection capability [25,26], are reported in this $MoSi_2N_4$ system, which are even superior to the MoS_2 one. Due to the protection of outlying SiN surface, the $MoSi_2N_4$ nanosheet can exhibit a tunable Schottky barrier at the metal/semiconductor contact [27], which would be a good air-stable channel material for the sub-5-nm MOSFETs [28]. Novel bilayer heterostructures can be created by coupling the $MoSi_2N_4$ nanosheet with other 2D systems, and the formed heterostructures present versatile electronic properties that can be further tuned by external strain and electric-field [29–32].

Analogous to the TMDs, the effects of TM elements on the electronic structures of MA_2Z_4 nanosheets have been highlighted by scientists [33,34]. For the MSi_2N_4 systems, they can be metallic or semiconducting depending on the valence electron counts (VECs) rather than the structural phases [35,36]. With even VECs, the group-IV/-VI MA_2Z_4 nanosheets are semiconductors, among which the $HfSi_2N_4$ one is identified as a promising candidate for photocatalytic CO_2 reduction [37–39]. On the other hand, the group-V MA_2Z_4 systems with odds VECs are metals, which are predicted as appealing electrocatalysts for the oxygen reduction and hydrogen evolution reactions [40–42]. The VSi_2N_4 system is even reported as a rare valley-half-semiconductor [43,44]. It would be noted that the MSi_2N_4 nanosheet can be regarded as a MN_2 nanosheet sandwiched between two SiN surfaces [45]. Thus, comparing to the TMDs, there will be a new degree, i.e the composition of surface layer, that can manipulate the electronic structures of MSi_2N_4

* Corresponding authors.
E-mail addresses: dingyi2001@tsinghua.org.cn (Y. Ding), wangyanli-04@tsinghua.org.cn (Y. Wang).

https://doi.org/10.1016/j.apsusc.2022.153317
Received 18 January 2022; Received in revised form 19 March 2022; Accepted 3 April 2022
Available online 12 April 2022

nanosheets. Following the design idea of atomic transmutation [46], the SiN surfaces would be replaced by the isoelectronic III–VI ones to form the $MN_2X_2Y_2$ nanosheet, which has the same VECs to the MSi_2N_4 one [47].

In the experiment, the $MoSi_2N_4$ nanosheet has been synthesized by the chemical vapour deposition (CVD) growth of molybdenum nitride with additional silicon substance [11]. Thus, it could be expected that the $MoN_2X_2Y_2$ nanosheets would be obtained by similar CVD method with appropriate III–VI additives. Besides that, in the literature, the analogous septuple-atomic-layer MX_2Y_4 materials, including $MnAl_2S_4$, $MnGa_2S_4$, $FeIn_2S_4$, $FeIn_2Se_4$, and $FeIn_2S_2Se_2$, have already been experimentally reported [48–50]. Thus, through the substitution reactions, the $MoN_2X_2Y_2$ nanosheets may also be produced from these layered MX_2Y_4 materials. However, two isostructural and isoelectronic systems may exhibit distinct electronic behaviours as in the case of graphene and BN nanosheets [51]. Thus, it can be expected that the $MN_2X_2Y_2$ systems will also possess peculiar electronic and magnetic properties. However, even for the $MoSi_2N_4$ one, the corresponding group III–VI derivatives have not been studied yet. How about the structural stability of these $MoN_2X_2Y_2$ nanosheets with different XY compositions? What kind of fascinating electronic properties will appear in these systems? When the $MoN_2X_2Y_2$ nanosheets are coupled with $MoSi_2N_4$ one, how will the heterostructures behave like? To address these issues, we perform a computational study to systematically investigate the structural stability, electronic and magnetic properties of $MoN_2X_2Y_2$ nanosheets.

2. Computational details

The first-principles calculations are performed by the VASP code [52], which utilizes Perdew–Burke–Ernzerhof (PBE) projector-augmented wave pseudo-potentials and plane-wave basis sets with a cut-off energy of 500 eV. The Brillouin zone is sampled by a Wisesa–McGill–Mueller k-grid with minimum period distances of 40 and 50 Åin the relaxation and static calculations, respectively [53]. The Grimme-D3 correction with Becke–Jonson damping is adopted for the van der Waals interaction in the bilayer systems [54]. A vacuum layer of about 15 Åis used to simulate the isolated 2D systems, and all the geometrical structures are fully relaxed until the maximum residual force is less than 0.01 eV/Å. The obtained electronic structures are also checked by the Heyd–Scuseria–Ernzerhof (HSE) functional, for which an interpolation of Wannier function is used to obtain the hybrid band structure [55]. The phonon spectra are calculated by the Phonopy code on a 5 × 5 supercell via the finite-displacement method [56], where a rotational sum rule is enforced on the force constants by the Hiphive package [57]. Ab initio molecular dynamic (AIMD) simulations are performed on a 4 × 4 supercell, which adopt the canonical NVT ensemble with a Nose thermostat of 300 K. The step time is set to 1 fs and the total simulated time is 5 ps, i.e. up to 5000 steps.

3. Results and discussion

Figs. 1(a) and (b) depict the geometrical structures of $MoN_2X_2Y_2$ nanosheets, which are derived from $MoSi_2N_4$ via the replacement of SiN surfaces by the isoelectronic III–VI XY ones. Here, all the possible combinations from group III and VI elements in the period 2–5 are considered, and there are sixteen $MoN_2X_2Y_2$ candidates. The corresponding geometrical and energetic information of these $MoN_2X_2Y_2$ nanosheets is provided in Figs. 1(c) and (d). Compared to the pristine $MoSi_2N_4$ system (a=2.908 Å, h=7.002 Å), most $MoN_2X_2Y_2$ nanosheets have longer lattice constants and bigger layer thickness. Through the phonon calculations, three $MoN_2X_2Y_2$ (XY=GaTe, InSe, InTe) nanosheets are filtered out due to the remarkable imaginary frequencies in their Brillouin zone. While all the other ones are dynamically stable as shown in Fig. S1 of supplementary material. Since in the literature, the MA_2Z_4 materials can be viewed as the 2H-phase MZ_2 nanosheet inserted between the InSe-type A_2Z_2 layers [33], the formation energy (E_{form}) of $MoN_2X_2Y_2$ nanosheets is calculated as $E_{form} = E_{MoN_2X_2Y_2} - E_{MoN_2} - E_{X_2Y_2}$, where $E_{MoN_2X_2Y_2}$ is the total energy of $MoN_2X_2Y_2$ nanosheet, E_{MoN_2} is the energy of the isolated MoN_2 nanosheet at the ferromagnetic state, and $E_{X_2Y_2}$ is the energy of the InSe-like III–VI X_2Y_2 nanosheet. According to this definition, a negative (positive) E_{form} corresponds to an exothermic (endothermic) synthesis process for the corresponding $MoN_2X_2Y_2$ nanosheet, which is energetically favourable (unfavourable) comparing to the isolated MoN_2 and X_2Y_2 layers. The obtained formation energies of $MoN_2X_2Y_2$ nanosheets are displayed in Fig. 1(d). It can be seen that among the thirteen dynamically stable systems, three $MoN_2X_2Y_2$ nanosheets (XY=AlTe, GaSe, InS) are energetically unfavourable due to their positive E_{form} values. For the remaining ten $MoN_2X_2Y_2$ systems, the AIMD simulations are further conducted to check their thermal stability. As indicated in Fig. S2 of supplementary material, except the $MoN_2B_2O_2$, all the other nine $MoN_2X_2Y_2$ systems are thermally stable at room temperature. The structural integrity is well kept during the AIMD simulations and the total energies are just fluctuated around the equilibrium values. After the AIMD simulations, there is no bond breaking and only small distortions appear in the final configuration, which can be recovered by the structural relaxation. Here, combined with the phonon, AIMD and formation energy results, good structural stability is confirmed in the nine $MoN_2X_2Y_2$ (XY=BS, BSe, BTe, AlO, AlS, AlSe, GaO, GaS, and InO) nanosheets, which can withstand the free-standing form at room temperature. This suggests those $MoN_2X_2Y_2$ nanosheets will be experimentally accessible like the $MoSi_2N_4$ system.

Regarding to the unstable $MoN_2X_2Y_2$ systems, the crystal orbital Hamilton population (COHP) bonding analysis are performed to get more insights into their instability. The integral value of –COHP up to the Fermi level (-ICOHP) are provided in the Tab. S1 of supplementary material. Here, the big (small) -ICOHP value corresponds to a strong (weak) bond [58,59]. It can be seen that for the dynamically unstable $MoN_2X_2Y_2$ nanosheets (XY=GaTe, InSe, InTe), their X–Y bonds are much weaker than the stable ones, which leads to the dynamical instability. While for the energetically unstable ones (XY=AlTe, GaSe, InS), the Mo–N, and N–X, and X–Y bonds are also weaker, which makes the system energetically unfavourable. For the thermally unstable $MoN_2B_2O_2$ nanosheet, although the -ICOHP value of B–O bond seems to be big, the corresponding bond length is as long as 1.64 Å, which is much larger than the common B–O bonds (1.28–1.43 Å) in the boron–oxygen materials [60]. This indicates that the B–O bonds are stretched significantly to accommodate the MoN_2 layer, which become largely weakened in the $MoN_2B_2O_2$ nanosheet. As a result, the regular BO hexagons will be broken during the 300 K AIMD simulation, and the surface layer is transformed to an amorphous morphology as shown in Fig. S3 of supplementary material. Thus, strong enough X–Y bonds with matched bond lengths to the MoN_2 layer are the prerequisite for the stability of $MoN_2X_2Y_2$ nanosheets.

Now, we pay main attention to the electronic structures of stable $MoN_2X_2Y_2$ nanosheets. The pristine $MoSi_2N_4$ nanosheet is an indirect-gap semiconductor, whose valence band maximum (VBM) is located at the Γ point and the conduction band minimum (CBM) lies at the K point [13]. Similar band features exist in the semiconducting $MoN_2X_2Y_2$ nanosheets as shown in Fig. 2, which are also indirect-gap semiconductors with the VBM and CBM at the Γ and K points, respectively. Through the analysis of orbital-resolved fat bands, it is found that the bands around the Fermi level are primarily originated from the Mo atoms. The Mo d_{z^2} orbital dominates the top valence band around the Γ and the bottom conduction band around the K point, while the Mo d_{xy/x^2-y^2} orbitals make an important contribution to the top valence band around the K point. These band compositions resemble the $MoSi_2N_4$ and MoS_2 cases [13]. Such fat band result is also consistent with the partial charge densities of band edges in Fig. 2(d). It can seen that the VBM is composed of the Mo d_{z^2} and N p_z orbitals and the CBM is made up of the Mo d_{z^2} orbital solely. For the $MoN_2X_2Y_2$ nanosheets, a linear relationship is present between

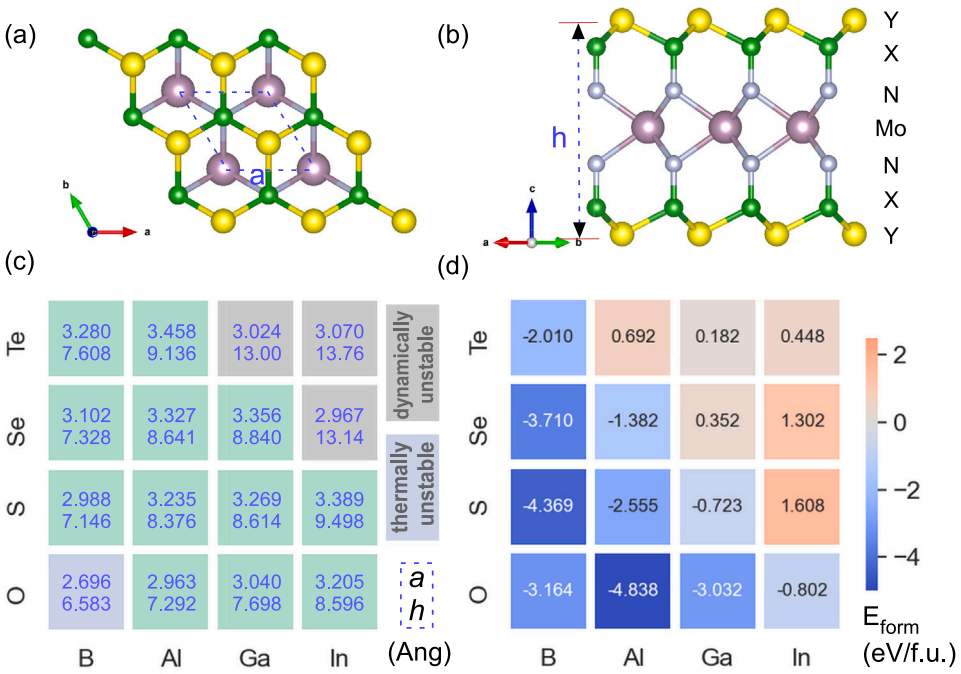

Fig. 1. (a) The top and (b) lateral view of $MoN_2X_2Y_2$ nanosheet. (c) The geometrical structures (lattice constant a and thickness h) and (d) energetic properties (formation energies E_{form}) of $MoN_2X_2Y_2$ nanosheets. The dynamically and thermally unstable systems are marked in (c).

the gap size and lattice constant as shown in Fig. 2(b). A long a value leads to a smaller band gap. This result is reasonable because the coupling between the Mo d_{z^2} and N p_z orbitals will be weakened in the case of a long lattice constant. As a result, the VBM and CBM, which are both dominated by the Mo d_{z^2} orbital, will approach each other and result in a reduced band gap. Such phenomenon has also been reported in the stretched $MoSi_2N_4$ nanosheet [61,62]. Here, due to the longer lattice constants, all the semiconducting $MoN_2X_2Y_2$ nanosheets have smaller band gaps than the $MoSi_2N_4$ one in Fig. 2(b). It will be noted that the linear relation will be deviated if the $MoN_2X_2Y_2$ systems become metallic. When the lattice constant exceeds 3.2 Å, the gap is closed in the $MoN_2X_2Y_2$ (XY=AlS, GaS, AlSe, BTe) nanosheets, which present a metallic behaviour by the PBE calculation. The HSE calculation predicts similar metallic feature in these systems except for the $MoN_2Al_2S_2$ nanosheet, which is still semiconducting with a small band gap of 0.023 eV from the HSE result. In view of the strong dependence of band gap on the lattice constant, it can be expected that the strain engineering can effectively tune the metallic behaviour of these $MoN_2X_2Y_2$ nanosheets. As indicated in Fig. 2(f), the overlap between the bottom conduction band at the K point and the top valence band at Γ point is decreased (increased) under the compressive (tensile) strains. For the $MoN_2Al_2S_2$ and $MoN_2Ga_2S_2$ nanosheets, the overlap can be diminished by small strains of about −0.02. Thus a metal–semiconductor transition can be easily triggered in these $MoN_2X_2Y_2$ nanosheets by small strains. Such critical strains are much smaller than the one required for the metal–semiconductor transition in the $MoSi_2N_4$ system (more than 10% for the bilayer case [63]), which are experimental affordable and endow those $MoN_2X_2Y_2$ systems promising nanomechanical sensor applications.

It would be noted that for the $MoN_2X_2Y_2$ (XY= AlO, GaO, InO) systems, their top valence bands are dispersionless around the Γ point. Taking the $MoN_2Al_2O_2$ nanosheet as an example in Fig. 3(a), a Mexican-hat-like band dispersion can be clearly visualized in the top valence band. A high peak is present in the density of states (DOSs), which causes a van Hove singularity in the valence band edge. Consequently, when the Fermi level is shifted into the DOSs peak through the hole doping, remarkable electron–electron repulsion will be present for the electrons at the Fermi surface. According to the Stoner theory [64], these electrons will prefer to be spin-polarized, which reduces the DOS at the Fermi level and further lowers the total energy. Thus, a spin-polarized calculation is performed to check the possible Stoner magnetism in the hole-doped $MoN_2Al_2O_2$ nanosheet. As shown in Fig. 3(b), the doped holes are fully spin-polarized when the hole concentration (q_h) is in the range of about $[0.5, 6] \times 10^{13}$ cm^{-2}. The corresponding energy gain from the spin-polarization (ΔE_s) is up to 2.8 meV/hole in this $MoN_2Al_2O_2$ nanosheet at $q_h = 4 \times 10^{13}$ cm^{-2}, which is comparable to the data of hole-doped GaS, GaSe, and InSe systems (2–3 meV/hole) [64,65] and is bigger than the GaTe and InTe ones (1 meV/hole) [65]. It would be noted that in the HSE calculation, the top valence band becomes flat around the Γ point as shown in Fig. 3(a). The valence band edge at the Γ point is merely 0.001 eV lower than the VBM, which makes the Mexican-hat-like dispersion feature less obvious than the PBE one. Such discrepancy between the PBE and HSE results will be attributed to the different rates of band components (see Fig. S4 of supplementary material). However, the flat band from the HSE calculation also produces a high DOS peak in the valence band edge, which facilitates hole-induced magnetism like the PBE case.

Accompanied with the magnetism, an intriguing half-metallic behaviour is present in the hole-doped $MoN_2Al_2O_2$ nanosheet. As shown in Fig. 3(c), there is a noticeable exchange splitting in the top valence band, which is 0.027/0.157 eV at the Γ point from the PBE/HSE result. Owing to the hole doping, the Fermi level only crosses the spin down valence band and causes a half-metallic behaviour. The half-metallic gap, which is the energy of topmost occupied band relative to the Fermi level, is 0.011/0.097 eV by the PBE/HSE calculation. In addition to the ferromagnetic coupling, the antiferromagnetic coupling is also examined for the doped $MoN_2Al_2O_2$ nanosheet. However, it always converges to the ferromagnetic coupling in the static calculation, confirming that the hole-doped $MoN_2Al_2O_2$ system possesses a stable ferromagnetic state. For the doped systems, the Curie temperature (T_c) is estimated by a mean-field theory approach [64,65]. The temperature effect is taken into account as a smearing factor in the Fermi–Dirac distribution function. Through minimizing the free energy of electrons at finite temperature, the T_c value can be evaluated from the dependence of magnetic moment on the temperature. As indicated in Fig. 3(d), the estimated T_c is 85 K in the hole-doped $MoN_2Al_2O_2$ nanosheet, which

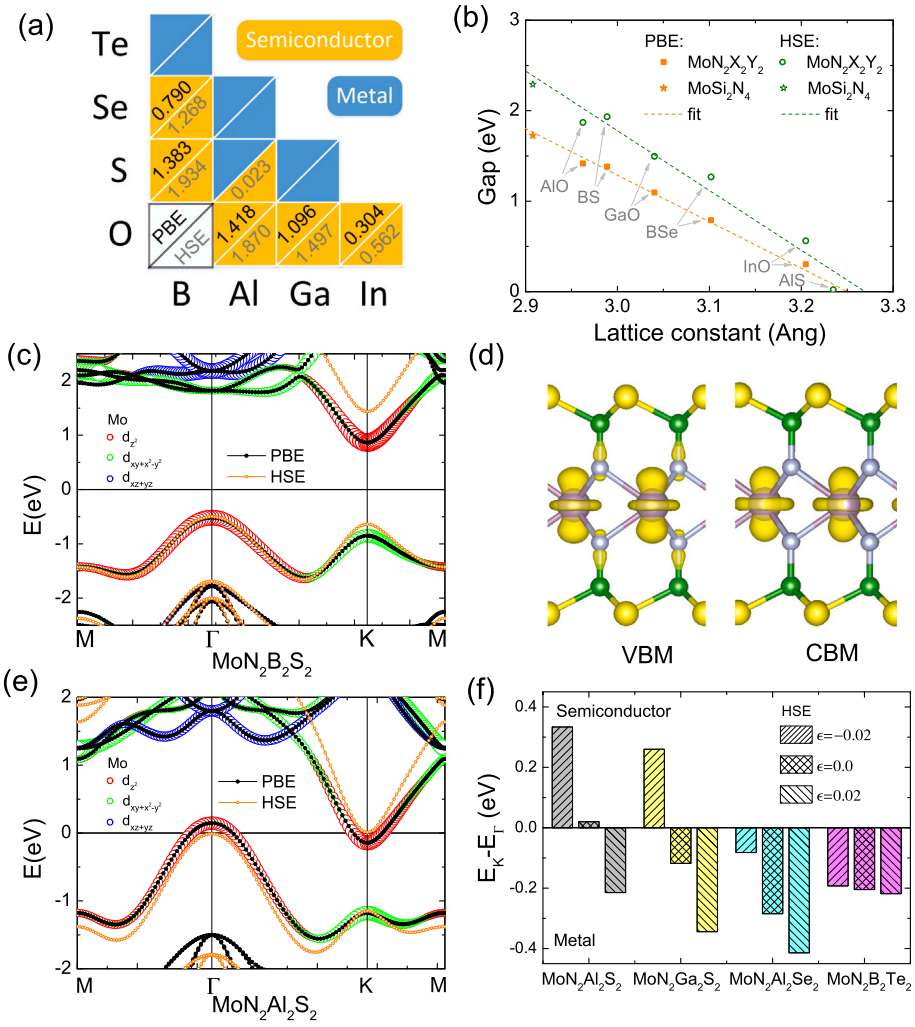

Fig. 2. (a) The electronic behaviours of stable $MoN_2X_2Y_2$ nanosheets, where the PBE/HSE gaps are also labelled out for the semiconductors. (b) The variation of gap size versus lattice constant in the $MoN_2X_2Y_2$ nanosheets. The orbital-resolved fat bands of (c) $MoN_2B_2S_2$ and (e) $MoN_2Al_2S_2$ nanosheets. (d) The partial charge densities of the VBM and CBM in the $MoN_2B_2S_2$ nanosheet. (f) The strain-induced gap variation of metallic $MoN_2X_2Y_2$ nanosheets. Here, E_K/E_Γ is the energy of bottom conduction/top valence band at the K/Γ point, and the positive (negative) energy difference between them means a semiconducting (metallic) feature in the corresponding $MoN_2X_2Y_2$ nanosheet.

is similar to the GaSe counterpart (91 K [64]). For the hole-doped $MoN_2Ga_2O_2$ and $MoN_2In_2O_2$ nanosheets, their maximum ΔE_s are 1.6 and 0.8 meV/hole and the corresponding T_c are 71 and 65 K as shown in Figs. 3(b) and (d), respectively. Thus, a low-temperature condition is required to realize the hole-doped ferromagnetism and half-metallicity in these $MoN_2X_2Y_2$ (XY= AlO, GaO, InO) nanosheets. Fortunately, the compressive strain, which makes the top valence band flatter, can help to increase T_c. For the $MoN_2Al_2O_2$ nanosheet, as indicated in Fig. 3(d), the T_c will be raised to 92 and 100 K under the biaxial compressive strains of −0.02 and −0.04, respectively. These T_c values are much higher than the liquid nitrogen temperature (77 K), which facilitates the experimental achievement of promising magnetic properties in the $MoN_2X_2Y_2$ nanosheets.

Finally, the stable $MoN_2X_2Y_2$ nanosheets also offer new building blocks for the van der Waals heterostructures (VDWHs) [66]. Since the lattice constants of $MoN_2Al_2O_2$ and $MoN_2B_2S_2$ nanosheets are close to the $MoSi_2N_4$ one, the lattice mismatches between them are less than 3%. Thus a commensurable bilayer structure can be constructed from their 1×1 unit cells. Following the convention of $MoSi_2N_4$ bilayers [67,68], five stacking geometries, including AA, AB, AB*, AC, AC*, are considered for the $MoN_2X_2Y_2$-$MoSi_2N_4$ VDWHs. The AB and AC stacking structures are found to be the most stable for the $MoN_2Al_2O_2$-$MoSi_2N_4$ and $MoN_2B_2S_2$-$MoSi_2N_4$ ones, respectively. The corresponding binding energies E_b, which are the energy differences between the heterostructure and isolated layers, are calculated as −0.222 and −0.212 eV/f.u. for them. These values correspond to an interlayer interaction of 30–28 meV/Å^2 in the $MoN_2X_2Y_2$-$MoSi_2N_4$ VDWHs, which is comparable to the common van der Waals interactions in layered compounds (~20 meV/Å^2) [69]. The band structures of $MoN_2X_2Y_2$-$MoSi_2N_4$ VDWHs are depicted in the Figs. 4(a) and (d). It can be seen that the bands of $MoN_2X_2Y_2$ and $MoSi_2N_4$ layers are clearly recognized. There is no interlayer hybridization between them around the Fermi level. For the $MoN_2B_2S_2$-$MoSi_2N_4$ VDWH, the top valence band is originated from the $MoN_2B_2S_2$ layer while the bottom conduction band is from the $MoSi_2N_4$ one. Thus, a staggered-gap type-II band alignment is formed in this $MoN_2B_2S_2$-$MoSi_2N_4$ VDWH. Similar band feature is also obtained in the $MoN_2Al_2O_2$-$MoSi_2N_4$ system, i.e. the top valence and bottom conduction bands are also originated from different layers. However, the top valence band at the Γ point is higher than the bottom conduction band at K point, which leads to a metallic behaviour. This stems from the big band offset between the isolated $MoN_2Al_2O_2$ and $MoSi_2N_4$ nanosheets, where the CBM of $MoSi_2N_4$ layer is even 0.189 eV lower than the VBM of $MoN_2Al_2O_2$ layer. Thus according to the Schottky–Mott rule [70–72], there will be a broken-gap type-III band alignment existing in the $MoN_2Al_2O_2$-$MoSi_2N_4$ VDWH. Interestingly, the band alignment of these $MoN_2X_2Y_2$-$MoSi_2N_4$ VDWHs can be further modulated by the strain. As shown in Figs. 4(b) and (e), the absolute energy of CBM

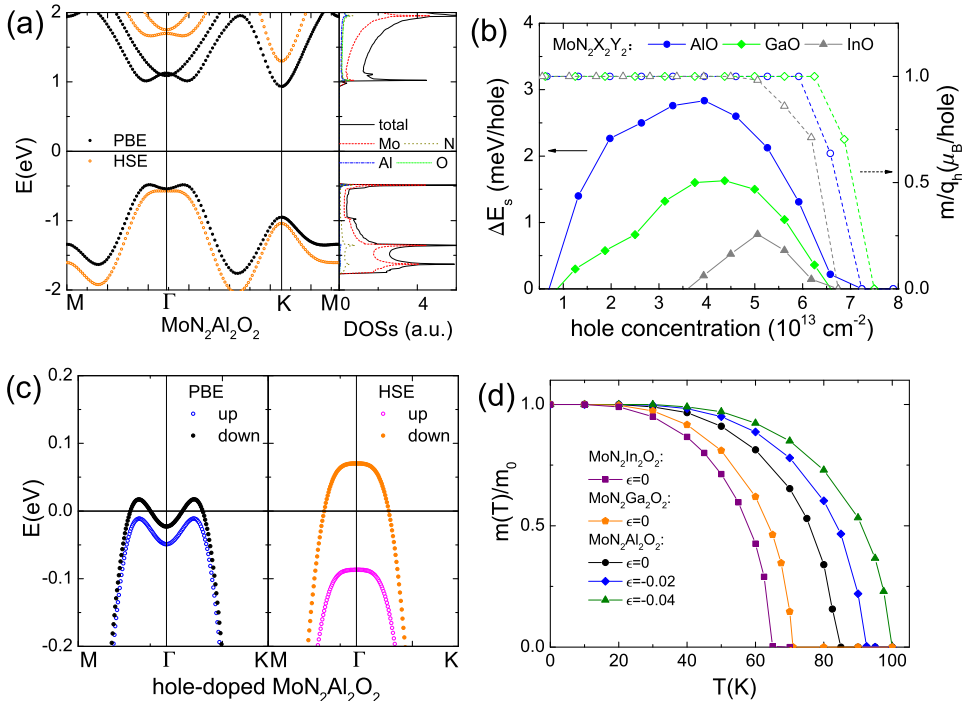

Fig. 3. (a) The PBE and HSE band structures of $MoN_2Al_2O_2$ nanosheet. (b) The spin-polarization energy and magnetic moment of hole-doped $MoN_2X_2Y_2$ (XY= AlO, GaO, InO) nanosheets. (c) The spin-polarized PBE and HSE band structures of hole-doped $MoN_2Al_2O_2$ nanosheet with the $q_h = 4\times10^{13}$ cm^{-2}. (d) The variation of the magnetic moment versus temperature in the $MoN_2X_2Y_2$ nanosheets.

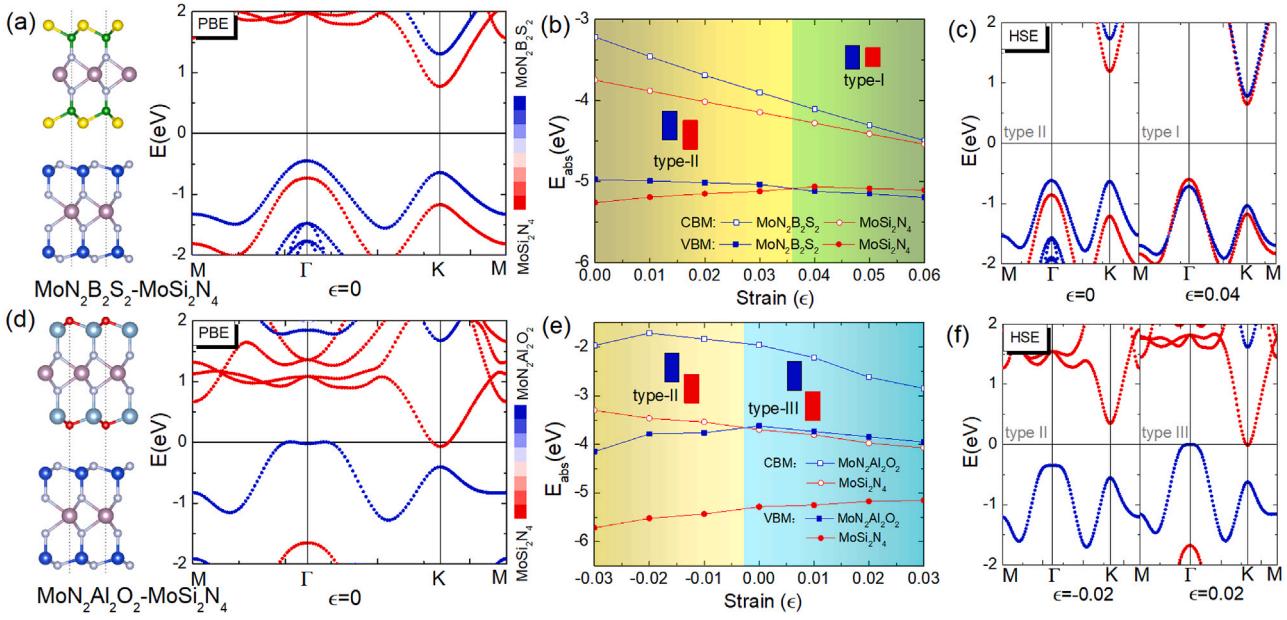

Fig. 4. [(a), (d)] The atomic structures and PBE band structures of $MoN_2B_2S_2$-$MoSi_2N_4$ and $MoN_2Al_2O_2$-$MoSi_2N_4$ heterostructures. [(b), (e)] The variations of absolute energies of band edges in different building layers versus strains. Here, the vacuum level is adopted as the zero points. [(c), (f)] The corresponding HSE band structures of strained $MoN_2B_2S_2$-$MoSi_2N_4$ and $MoN_2Al_2O_2$-$MoSi_2N_4$ heterostructures.

is lowered (raised) by the tensile (compressive) strain, while the VBM presents a converse variation trend. Thus for the $MoN_2Al_2O_2$-$MoSi_2N_4$ VDWH, a compressive strain of $\varepsilon \leq -0.01$ will shift the CBM above the VBM and transform the system into a type-II band alignment. While in the $MoN_2B_2S_2$-$MoSi_2N_4$ system, the variations of band edge in the $MoSi_2N_4$ layer are more pronounced than the $MoN_2B_2S_2$ one. Consequently, a transition from the type-II to type-I band alignment is present in the $MoN_2B_2S_2$-$MoSi_2N_4$ VDWH under the tensile strain of $\varepsilon \geq 0.04$. To verify these band alignment transformations, the HSE calculations are performed on the $MoN_2X_2Y_2$-$MoSi_2N_4$ VDWHs. As in Figs. 4 (c) and (f), the HSE results are consistent with the PBE ones that all the band alignment types, including type I, II, and III, can emerge in

the strained $MoN_2X_2Y_2$-$MoSi_2N_4$ systems. Therefore, these $MoN_2X_2Y_2$-$MoSi_2N_4$ VDWHs will be promising platforms to achieve multiple band alignments for nanoscale electronic devices.

4. Conclusion

In summary, we have performed a comprehensive first-principles study on the group III–VI $MoN_2X_2Y_2$ nanosheets, which are the isostructural and isoelectronic analogues of $MoSi_2N_4$ system. It is found that (1) among the sixteen candidates, there are nine III–VI XY combinations that can form stable $MoN_2X_2Y_2$ nanosheets, which possess robust dynamical, energetic, and thermal stability. (2) These $MoN_2X_2Y_2$ nanosheets can be indirect-gap semiconductors or metals depending on the XY compositions. For the semiconducting systems, a linear relationship is present between the band gap and lattice constant. Regarding to the metallic ones with XY=AlS, GaS, a metal–semiconductor transition can be easily triggered by small strains. (3) In particular, the Mexican-hat-like valence bands emerge in three $MoN_2X_2Y_2$ (XY=AlO, GaO, InO) nanosheets, which can be converted into ferromagnetic half-metals via the hole doping. (4) When the $MoN_2X_2Y_2$ (XY=BS, AlO) nanosheets are coupled with the $MoSi_2N_4$ system, the formed van der Waals heterostructures exhibit versatile and strain-tunable band alignments, including the straddling-gap type-I, staggered-gap type-II, and broken-gap type-III ones. Our study demonstrates the variation of surface layer provides a new degree to tailor the electronic structures of MA_2Z_4-based materials, which enable them intriguing nano-electrics, spintronics and device applications.

CRediT authorship contribution statement

Yi Ding: Conceptualization, Methodology, Writing – original draft. **Yanli Wang:** Software, Writing – review & editing.

Declaration of competing interest

The authors declare that they have no known competing financial interests or personal relationships that could have appeared to influence the work reported in this paper.

Acknowledgements

The authors acknowledge the support from the National Natural Science Foundation of China (11774312). Partial computations in this paper were run on the computational condensed matter physics cluster in the school of physics, hangzhou normal university.

Appendix A. Supplementary data

Supplementary material related to this article can be found online at https://doi.org/10.1016/j.apsusc.2022.153317.

References

[1] C. Tan, H. Zhang, Two-dimensional transition metal dichalcogenide nanosheet-based composites, Chem. Soc. Rev. 44 (2015) 2713–2731, http://dx.doi.org/10.1039/c4cs00182f.

[2] S. Manzeli, D. Ovchinnikov, D. Pasquier, O.V. Yazyev, A. Kis, 2D transition metal dichalcogenides, Nat. Rev. Mater. 2 (2017) 17033, http://dx.doi.org/10.1038/natrevmats.2017.33.

[3] F. Wu, C. Huang, H. Wu, C. Lee, K. Deng, E. Kan, P. Jena, Atomically thin transition-metal dinitrides: High-temperature ferromagnetism and half-metallicity, Nano Lett. 15 (2015) 8277–8281, http://dx.doi.org/10.1021/acs.nanolett.5b03835.

[4] J. Liu, Z. Liu, T. Song, X. Cui, Computational search for two-dimensional intrinsic half-metals in transition-metal dinitrides, J. Mater. Chem. C 5 (2017) 727–732, http://dx.doi.org/10.1039/c6tc04490e.

[5] H. Yuan, Z. Li, J. Yang, Transition-metal diboride: A new family of two-dimensional materials designed for selective CO_2 electroreduction, J. Phys. Chem. C 123 (2019) 16294–16299, http://dx.doi.org/10.1021/acs.jpcc.9b04221.

[6] M. Magnuson, L. Hultman, H. Högberg, Review of transition-metal diboride thin films, Vacuum 196 (2021) 110567, http://dx.doi.org/10.1016/j.vacuum.2021.110567.

[7] Q. Wu, Y. Zhang, Q. Zhou, J. Wang, X.C. Zeng, Transition-metal dihydride monolayers: A new family of two-dimensional ferromagnetic materials with intrinsic room-temperature half-metallicity, J. Phys. Chem. Lett. 9 (2018) 4260–4266, http://dx.doi.org/10.1021/acs.jpclett.8b01976.

[8] H. Lv, D. Wu, X. Li, X. Wu, J. Yang, Two-dimensional transitional metal dihydride crystals with anisotropic and spin-polarized Fermi Dirac cones, J. Mater. Chem. C 6 (2018) 11243–11247, http://dx.doi.org/10.1039/c8tc03489c.

[9] X. Jiang, A.V. Kuklin, A. Baev, Y. Ge, H. Ågren, H. Zhang, P.N. Prasad, Two-dimensional MXenes: From morphological to optical, electric, and magnetic properties and applications, Phys. Rep. 848 (2020) 1–58, http://dx.doi.org/10.1016/j.physrep.2019.12.006.

[10] W. Meng, X. Liu, H. Song, Y. Xie, X. Shi, M. Dargusch, Z.-G. Chen, Z. Tang, S. Lu, Advances and challenges in 2D mxenes: From structures to energy storage and conversions, Nano Today 40 (2021) 101273, http://dx.doi.org/10.1016/j.nantod.2021.101273.

[11] Y.-L. Hong, Z. Liu, L. Wang, T. Zhou, W. Ma, C. Xu, S. Feng, L. Chen, M.-L. Chen, D.-M. Sun, X.-Q. Chen, H.-M. Cheng, W. Ren, Chemical vapor deposition of layered two-dimension $MoSi_2N_4$ materials, Science 369 (2020) 670–674, http://dx.doi.org/10.1126/science.abb7023.

[12] K.S. Novoselov, Discovery of 2D van der Waals layered $MoSi_2N_4$ family, Natl. Sci. Rev. 7 (2020) 1842–1844, http://dx.doi.org/10.1093/nsr/nwaa190.

[13] A. Bafekry, M. Faraji, D.M. Hoat, M. Shahrokhi, M.M. Fadlallah, F. Shojaei, S.A.H. Feghhi, M. Ghergherehchi, D. Gogova, $MoSi_2N_4$ single-layer: a novel two-dimensional material with outstanding mechanical, thermal, electronic and optical properties, J. Phys. D: Appl. Phys. 54 (2021) 155303, http://dx.doi.org/10.1088/1361-6463/abdb6b.

[14] H. Yao, C. Zhang, Q. Wang, J. Li, Y. Yu, F. Xu, B. Wang, Y. Wei, Novel two-dimensional layered $MoSi_2Z_4$ (Z=P, As): New promising optoelectronic materials, Nanomaterials 11 (2021) 559, http://dx.doi.org/10.3390/nano11030559.

[15] R. Islam, B. Ghosh, C. Autieri, S. Chowdhury, A. Bansil, A. Agarwal, B. Singh, Tunable spin polarization and electronic structure of bottom-up synthesized $MoSi_2N_4$ materials, Phys. Rev. B 104 (2021) L201112, http://dx.doi.org/10.1103/physrevb.104.l201112.

[16] S. Li, W. Wu, X. Feng, S. Guan, W. Feng, Y. Yao, S.A. Yang, Valley-dependent properties of monolayer $MoSi_2N_4$, WSi_2N_4, and $MoSi_2As_4$, Phys. Rev. B 102 (2020) 235435, http://dx.doi.org/10.1103/physrevb.102.235435.

[17] C. Yang, Z. Song, X. Sun, J. Lu, Valley pseudospin in monolayer $MoSi_2N_4$ and $MoSi_2As_4$, Phys. Rev. B 103 (2021) 035308, http://dx.doi.org/10.1103/physrevb.103.035308.

[18] S.-D. Guo, Y.-T. Zhu, W.-Q. Mu, W.-C. Ren, Intrinsic piezoelectricity in monolayer MSi_2N_4 (M=Mo, W, Cr, Ti, Zr and Hf), EPL (Europhys. Lett.) 132 (2020) 57002, http://dx.doi.org/10.1209/0295-5075/132/57002.

[19] B. Mortazavi, B. Javvaji, F. Shojaei, T. Rabczuk, A.V. Shapeev, X. Zhuang, Exceptional piezoelectricity, high thermal conductivity and stiffness and promising photocatalysis in two-dimensional $MoSi_2N_4$ family confirmed by first-principles, Nano Energy 82 (2021) 105716, http://dx.doi.org/10.1016/j.nanoen.2020.105716.

[20] J. Yu, J. Zhou, X. Wan, Q. Li, High intrinsic lattice thermal conductivity in monolayer $MoSi_2N_4$, New J. Phys. 23 (2021) 033005, http://dx.doi.org/10.1088/1367-2630/abe8f7.

[21] Y. Yin, M. Yi, W. Guo, High and anomalous thermal conductivity in monolayer MSi_2Z_4 semiconductors, ACS Appl. Mater. Inter. 13 (2021) 45907–45915, http://dx.doi.org/10.1021/acsami.1c14205.

[22] C. Xiao, R. Sa, Z. Cui, S. Gao, W. Du, X. Sun, X. Zhang, Q. Li, Z. Ma, Enhancing the hydrogen evolution reaction by non-precious transition metal (non-metal) atom doping in defective $MoSi_2N_4$ monolayer, Appl. Surf. Sci. 563 (2021) 150388, http://dx.doi.org/10.1016/j.apsusc.2021.150388.

[23] Y. Zang, Q. Wu, W. Du, Y. Dai, B. Huang, Y. Ma, Activating electrocatalytic hydrogen evolution performance of two-dimensional MSi_2N_4(M=Mo, W) : A theoretical prediction, Phys. Rev. Mater. 5 (2021) 045801, http://dx.doi.org/10.1103/physrevmaterials.5.045801.

[24] W. Qian, Z. Chen, J. Zhang, L. Yin, Monolayer $MoSi_2N_4$- as promising electrocatalyst for hydrogen evolution reaction: A DFT prediction, J. Mater. Sci. Technol. 99 (2022) 215–222, http://dx.doi.org/10.1016/j.jmst.2021.06.004.

[25] A. Bafekry, M. Faraji, M. Fadlallah, A.A. Ziabari, A.B. Khatibani, S. Feghhi, M. Ghergherehchi, D. Gogova, Adsorption of habitat and industry-relevant molecules on the $MoSi_2N_4$ monolayer, Appl. Surf. Sci. 564 (2021) 150326, http://dx.doi.org/10.1016/j.apsusc.2021.150326.

[26] Z. Cui, Y. Luo, J. Yu, Y. Xu, Tuning the electronic properties of $MoSi_2N_4$ by molecular doping: A first principles investigation, Phys. E 134 (2021) 114873, http://dx.doi.org/10.1016/j.physe.2021.114873.

[27] Q. Wang, L. Cao, S.-J. Liang, W. Wu, G. Wang, C.H. Lee, W.L. Ong, H.Y. Yang, L.K. Ang, S.A. Yang, Y.S. Ang, Efficient Ohmic contacts and built-in atomic sublayer protection in $MoSi_2N_4$ and WSi_2N_4 monolayers, Npj 2D Mater. Appl. 5 (2021) 71, http://dx.doi.org/10.1038/s41699-021-00251-y.

[28] J. Huang, P. Li, X. Ren, Z.-X. Guo, Promising properties of a sub-5-nm monolayer $MoSi_2N_4$ transistor, Phys. Rev. Appl. 16 (2021) 044022, http://dx.doi.org/10.1103/PhysRevApplied.16.044022.

[29] J. Zhao, X. Jin, H. Zeng, C. Yao, G. Yan, Spin-valley coupling and valley splitting in the $MoSi_2N_4/CrCl_3$ van der Waals heterostructure, Appl. Phys. Lett. 119 (2021) 213101, http://dx.doi.org/10.1063/5.0072266.

[30] K.D. Pham, C.Q. Nguyen, C.V. Nguyen, P.V. Cuong, N.V. Hieu, Two-dimensional van der Waals graphene/transition metal nitride heterostructures as promising high-performance nanodevices, New J. Chem. 45 (2021) 5509–5516, http://dx.doi.org/10.1039/d1nj00374g.

[31] J. Zeng, L. Xu, Y. Yang, X. Luo, H.-J. Li, S.X. Xiong, L.-L. Wang, Boosting the photocatalytic hydrogen evolution performance of monolayer C_2N coupled with $MoSi_2N_4$: density-functional theory calculations, Phys. Chem. Chem. Phys. 23 (2021) 8318–8325, http://dx.doi.org/10.1039/d1cp00364j.

[32] J. Zhao, Y. Zhao, H. He, P. Zhou, Y. Liang, T. Frauenheim, Stacking engineering: A boosting strategy for 2D photocatalysts, J. Phys. Chem. Lett. 12 (2021) 10190–10196, http://dx.doi.org/10.1021/acs.jpclett.1c03089.

[33] L. Wang, Y. Shi, M. Liu, A. Zhang, Y.-L. Hong, R. Li, Q. Gao, M. Chen, W. Ren, H.-M. Cheng, Y. Li, X.-Q. Chen, Intercalated architecture of MA_2Z_4 family layered van der Waals materials with emerging topological, magnetic and superconducting properties, Nature Commun. 12 (2021) 2361, http://dx.doi.org/10.1038/s41467-021-22324-8.

[34] J. Chen, Q. Tang, The versatile electronic, magnetic and photo-electro catalytic activity of a new 2D MA_2Z_4 family, Chem. Eur. J. 27 (2021) 9925–9933., http://dx.doi.org/10.1002/chem.202100851.

[35] Y. Wang, Y. Ding, Computational exploration of stable 4D/5D transition-metal MSi_2N_4 (M=Y-Cd and Hf-Hg) nanosheets and their versatile electronic and magnetic properties, J. Phys. Chem. C 125 (2021) 19580–19591, http://dx.doi.org/10.1021/acs.jpcc.1c06734.

[36] W. Zhou, L. Wu, A. Li, B. Zhang, F. Ouyang, Structural symmetry, spin–orbit coupling, and valley-related properties of monolayer WSi_2N_4 family, J. Phys. Chem. Lett. 12 (2021) 11622–11628, http://dx.doi.org/10.1021/acs.jpclett.1c03197.

[37] A. Yadav, J. Kangsabanik, N. Singh, A. Alam, Novel two-dimensional MA_2N_4 materials for photovoltaic and spintronic applications, J. Phys. Chem. Lett. 12 (2021) 10120–10127, http://dx.doi.org/10.1021/acs.jpclett.1c02650.

[38] B. Mortazavi, F. Shojaei, B. Javvaji, T. Rabczuk, X. Zhuang, Outstandingly high thermal conductivity, elastic modulus, carrier mobility and piezoelectricity in two-dimensional semiconducting CrC2N4: a first-principles study, Mater. Today Energy 22 (2021) 100839, http://dx.doi.org/10.1016/j.mtener.2021.100839.

[39] Y. Liu, T. Zhang, K. Dou, W. Du, R. Peng, Y. Dai, B. Huang, Y. Ma, Valley-contrasting physics in single-layer $CrSi_2N_4$ and $CrSi_2P_4$, J. Phys. Chem. Lett. (2021) 8341–8346, http://dx.doi.org/10.1021/acs.jpclett.1c02069.

[40] Y. Chen, S. Tian, Q. Tang, First-principles studies on electrocatalytic activity of novel two-dimensional MA_2Z_4 monolayers toward oxygen reduction reaction, J. Phys. Chem. C 125 (2021) 22581–22590, http://dx.doi.org/10.1021/acs.jpcc.1c07044.

[41] J. Zheng, X. Sun, J. Hu, S. Wang, Z. Yao, S. Deng, X. Pan, Z. Pan, J. Wang, Symbolic transformer accelerating machine learning screening of hydrogen and deuterium evolution reaction catalysts in MA_2Z_4 materials, ACS Appl. Mater. Inter. 13 (2021) 50878–50891, http://dx.doi.org/10.1021/acsami.1c13236.

[42] Y. Liu, Y. Ji, Y. Li, Multilevel theoretical screening of novel two-dimensional MA_2Z_4 family for hydrogen evolution, J. Phys. Chem. Lett. 12 (2021) 9149–9154, http://dx.doi.org/10.1021/acs.jpclett.1c02487.

[43] X. Zhou, R.-W. Zhang, Z. Zhang, W. Feng, Y. Mokrousov, Y. Yao, Sign-reversible valley-dependent berry phase effects in 2D valley-half-semiconductors, Npj Comput. Mater. 7 (2021) 160, http://dx.doi.org/10.1038/s41524-021-00632-3.

[44] X. Feng, X. Xu, Z. He, R. Peng, Y. Dai, B. Huang, Y. Ma, Valley-related multiple Hall effect in monolayer VSi_2P_4, Phys. Rev. B 104 (2021) 075421, http://dx.doi.org/10.1103/physrevb.104.075421.

[45] L. Yan, B.-T. Wang, X. Huang, Q. Li, K. Xue, J. Zhang, W. Ren, L. Zhou, Surface passivation induced a significant enhancement of superconductivity in layered two-dimensional MSi_2N_4 (M=Ta and Nb) materials, Nanoscale 13 (2021) 18947–18954, http://dx.doi.org/10.1039/d1nr05560g.

[46] J.-H. Yang, Y. Zhang, W.-J. Yin, X.G. Gong, B.I. Yakobson, S.-H. Wei, Two-dimensional SiS layers with promising electronic and optoelectronic properties: Theoretical prediction, Nano Lett. 16 (2016) 1110–1117, http://dx.doi.org/10.1021/acs.nanolett.5b04341.

[47] Y. Wang, Y. Ding, Switchable valley polarization and quantum anomalous hall state in the $VN_2X_2Y_2$ nanosheets (X=group-III and Y=group-VI elements), Appl. Phys. Lett. 119 (2021) 193101, http://dx.doi.org/10.1063/5.0072220.

[48] M. Yokota, Y. Syono, S. Minomura, High-pressure phase transformations in $MnAl_2S_4$ and $MnGa_2s_4$, J. Solid State Chem. 3 (1971) 520–524, http://dx.doi.org/10.1016/0022-4596(71)90096-x.

[49] G. Goya, A. Memo, H. Haeuseler, Magnetic and Mossbauer study of the novel $FeIn_2S_2Se_2$ layered compound, J. Solid State Chem. 164 (2002) 326–331, http://dx.doi.org/10.1006/jssc.2001.9479.

[50] I.V. Bodnar, S.A. Detkov, Y.V. Kasyuk, Y.A. Fedotova, On the growth of $FeIn_2S_2Se_2$ single crystals and the study of their properties, Semiconductors 52 (2018) 1323–1326, http://dx.doi.org/10.1134/s1063782618100032.

[51] Z. Han, M. Li, L. Li, F. Jiao, Z. Wei, D. Geng, W. Hu, When graphene meets white graphene – recent advances in the construction of graphene and h-BN heterostructures, Nanoscale 13 (2021) 13174–13194, http://dx.doi.org/10.1039/d1nr03733a.

[52] G. Kresse, J. Furthmüller, Efficient iterative schemes for ab initio total-energy calculations using a plane-wave basis set, Phys. Rev. B 54 (1996) 11169–11186, http://dx.doi.org/10.1103/PhysRevB.54.11169.

[53] P. Wisesa, K.A. McGill, T. Mueller, Efficient generation of generalized Monkhorst-pack grids through the use of informatics, Phys. Rev. B 93 (2016) 155109, http://dx.doi.org/10.1103/PhysRevB.93.155109.

[54] S. Grimme, S. Ehrlich, L. Goerigk, Effect of the damping function in dispersion corrected density functional theory, J. Comput. Chem. 32 (2011) 1456–1465, http://dx.doi.org/10.1002/jcc.21759.

[55] G. Pizzi, V. Vitale, R. Arita, S. Blgel, F. Freimuth, G. Géranton, M. Gibertini, D. Gresch, C. Johnson, T. Koretsune, J.I. nez Azpiroz, H. Lee, J.-M. Lihm, D. Marchand, A. Marrazzo, Y. Mokrousov, J.I. Mustafa, Y. Nohara, Y. Nomura, L. Paulatto, S. Poncé, T. Ponweiser, J. Qiao, F. Thle, S.S. Tsirkin, M. Wierzbowska, N. Marzari, D. Vanderbilt, I. Souza, A.A. Mostofi, J.R. Yates, Wannier90 as a community code: new features and applications, J. Phys.: Condens. Matter 32 (2020) 165902, http://dx.doi.org/10.1088/1361-648x/ab51ff.

[56] A. Togo, I. Tanaka, First principles phonon calculations in materials science, Scr. Mater. 108 (2015) 1–5.

[57] F. Eriksson, E. Fransson, P. Erhart, The hiphive package for the extraction of high-order force constants by machine learning, Adv. Theor. Simul. 2 (2019) 1800184, http://dx.doi.org/10.1002/adts.201800184.

[58] V.L. Deringer, A.L. Tchougréeff, R. Dronskowski, Crystal orbital hamilton population (COHP) analysis as projected from plane-wave basis sets, J. Phys. Chem. A 115 (2011) 5461–5466, http://dx.doi.org/10.1021/jp202489s.

[59] R. Nelson, C. Ertural, J. George, V.L. Deringer, G. Hautier, R. Dronskowski, LOBSTER : Local orbital projections, atomic charges, and chemical-bonding analysis from projector-augmented-wave-based density-functional theory, J. Comput. Chem. 41 (2020) 1931–1940, http://dx.doi.org/10.1002/jcc.26353.

[60] C.A. Coulson, T.W. Dingle, The B-O bond lengths in boron-oxygen compounds, Acta Crystallogr. Sect. B 24 (1968) 153–155, http://dx.doi.org/10.1107/s0567740868001846.

[61] C. Jian, X. Ma, J. Zhang, X. Yong, Strained $MoSi_2N_4$ monolayers with excellent solar energy absorption and carrier transport properties, J. Phys. Chem. C 125 (2021) 15185–15193, http://dx.doi.org/10.1021/acs.jpcc.1c03585.

[62] X. Lv, Y. Xu, B. Mao, G. Liu, G. Zhao, J. Yang, Strain modulation of electronic and optical properties of monolayer $MoSi_2N_4$, Phys. E 135 (2022) 114964, http://dx.doi.org/10.1016/j.physe.2021.114964.

[63] Q. Wu, L. Cao, Y.S. Ang, L.K. Ang, Semiconductor-to-metal transition in bilayer $MoSi_2N_4$ and WSi_2N_4 with strain and electric field, Appl. Phys. Lett. 118 (2021) 113102, http://dx.doi.org/10.1063/5.0044431.

[64] T. Cao, Z. Li, S.G. Louie, Tunable magnetism and half-metallicity in hole-doped monolayer GaSe, Phys. Rev. Lett. 114 (2015) 236602, http://dx.doi.org/10.1103/PhysRevLett.114.236602.

[65] W. Feng, G.-Y. Guo, Y. Yao, Tunable magneto-optical effects in hole-doped group-IIIA metal-monochalcogenide monolayers, 2D Mater. 4 (2016) 015017, http://dx.doi.org/10.1088/2053-1583/4/1/015017.

[66] A.K. Geim, I.V. Grigorieva, Van der Waals heterostructures, Nature 499 (2013) 419–425, http://dx.doi.org/10.1038/nature12385.

[67] H. Zhong, W. Xiong, P. Lv, J. Yu, S. Yuan, Strain-induced semiconductor to metal transition in MA_2Z_4 bilayers (M=Ti,Cr,Mo; A=Si; Z=N,P), Phys. Rev. B 103 (2021) 085124, http://dx.doi.org/10.1103/physrevb.103.085124.

[68] A. Bafekry, C. Stampfl, M. Naseri, M.M. Fadlallah, M. Faraji, M. Ghergherehchi, D. Gogova, S.A.H. Feghhi, Effect of electric field and vertical strain on the electro-optical properties of the MoSi2N4 bilayer: A first-principles calculation, J. Appl. Phys. 129 (2021) 155103, http://dx.doi.org/10.1063/5.0044976.

[69] T. Björkman, A. Gulans, A.V. Krasheninnikov, R.M. Nieminen, Van der Waals bonding in layered compounds from advanced density-functional first-principles calculations, Phys. Rev. Lett. 108 (2012) 235502, http://dx.doi.org/10.1103/PhysRevLett.108.235502.

[70] L. Cao, G. Zhou, Q. Wang, L.K. Ang, Y.S. Ang, Two-dimensional van der Waals electrical contact to monolayer $MoSi_2N_4$, Appl. Phys. Lett. 118 (2021) 013106, http://dx.doi.org/10.1063/5.0033241.

[71] Y. Wang, Y. Ding, The electronic structures of group-V–group-IV heterobilayer structures: a first-principles study, Phys. Chem. Chem. Phys. 17 (2015) 27769–27776, http://dx.doi.org/10.1039/c5cp04815j.

[72] C. Nguyen, N.V. Hoang, H.V. Phuc, A.Y. Sin, C.V. Nguyen, Two-dimensional Boron phosphide/$MoGe_2N_4$ van der Waals heterostructure: A promising tunable optoelectronic material, J. Phys. Chem. Lett. 12 (2021) 5076–5084, http://dx.doi.org/10.1021/acs.jpclett.1c01284.